Journal of Geophysical Research: Atmospheres

RESEARCH ARTICLE
10.1029/2018JD028727

This article is a companion to Dong et al. (2016) https://doi.org/10.1002/2016JD024941.

Key Points:
- Convective rain and stratiform rain have distinct N_{0E}-λ_E relationship, the former features constant N_{0E} and the latter with constant λ_E
- The subset of spectrum has strong impact on the DSD Gamma fitting
- By using the constant λ_E assumption, the overestimation issue in CR rain rate retrieval based on *Z-R* relationship can be greatly mitigated

Correspondence to:
X. Dong,
xdong@email.arizona.edu

Citation:
Wang, J., Dong, X., & Xi, B. (2018). Investigation of liquid cloud microphysical properties of deep convective systems: 2. Parameterization of raindrop size distribution and its application for convective rain estimation. *Journal of Geophysical Research: Atmospheres*, *123*, 11,637–11,651. https://doi.org/10.1029/2018JD028727

Received 27 MAR 2018
Accepted 21 SEP 2018
Accepted article online 4 OCT 2018
Published online 24 OCT 2018

Investigation of Liquid Cloud Microphysical Properties of Deep Convective Systems: 2. Parameterization of Raindrop Size Distribution and its Application for Convective Rain Estimation

Jingyu Wang[1,2], Xiquan Dong[1], and Baike Xi[1]

[1]Department of Hydrology and Atmospheric Sciences, University of Arizona, Tucson, AZ, USA, [2]Pacific Northwest National Laboratory, Richland, WA, USA

Abstract The liquid cloud microphysical properties for stratiform rain (SR) have been investigated in Part 1 of this series. Since convective rain (CR) has characteristics in raindrop size distribution (DSD) and precipitation that are distinct from SR, we investigate the CR properties in this study by using 20 hr of CR samples collected by 17 Automatic Parsivel Units disdrometers during the Midlatitude Continental Convective Clouds Experiment over the Atmospheric Radiation Measurement Southern Great Plains site. A full spectrum of DSD is constructed based on a total of 23 size channels (0.321 to 9.785 mm), and both Gamma and Exponential fitted functions are applied to extract the DSD shape parameters. Compared to SR properties, CR has distinct features including broader size range and narrower exponential slope parameter (λ_E). These results indicate that the assumption of constant exponential intercept parameter (N_{0E}) is inappropriate for CR rain rate estimates. Additionally, the subsetting scheme of the CR DSD spectra also has a strong impact on the Gamma/Exponential functions. Therefore, a new CR DSD parameterization scheme is developed by choosing the appropriate spectra subset with the constraint of rain rate and using the constant λ_E instead of constant N_{0E}. With the input of the radar reflectivity at the lowest observed height, the newly calculated CR rain rates match well with the collocated surface rain gauge measurements (127 Mesonet stations and 17 Automatic Parsivel Units), while the rain rates calculated using traditional *Z-R* relationship are 3–4 times larger, indicating that constant λ_E is a better assumption for CR DSD.

1. Introduction

Deep convective systems (DCSs) play a significant role both in global climate and local hydrological systems (e.g., Feng et al., 2011, 2012; Futyan & Del Genio, 2007), as the convection-related precipitation contributes up to 60% of annual total precipitation in the central United States (Ashley et al., 2003; Fritsch et al., 1986). Through the combination of Next-Generation Radar (NEXRAD) radar and Geostationary Operational Environmental Satellite observations, a hybrid cloud classification method was developed by Feng et al. (2011), and the DCSs were objectively classified into components of convective core (CC), stratiform rain (SR), and anvil clouds (AC) regions. This classification is critical because different portions of a DCS feature different precipitation properties and should be investigated separately. For example, Feng et al. (2011) found that the SR accounts for light and moderate rainfall and large spatial coverage and can last more than 10 hr, while the convective rain (CR) rain rates can be 1 order of magnitude higher than SR rain rate, causing a surge in accumulated precipitation amount within a short time period.

Over the past few decades, the CR characteristics have been investigated through different platforms, such as surface-based disdrometers and radar observations (e.g., Cao et al., 2008; Cao & Zhang, 2009; Joss & Waldvogel, 1990; Sauvageot, 1994; Zhang et al., 2011, 2016) and satellite observations (e.g., Tropical Rainfall Measuring Mission precipitation product (TRMM; Houze et al., 2015; Schumacher & Houze, 2003), and Self-Calibrating Multivariate Precipitation Retrieval (SCaMPR; Kuligowski, 2010; Stenz et al., 2014). Although the surface in situ measurements can provide detailed raindrop size distribution (DSD) information, their limited sampling area and scarce distribution make the long-term statistics difficult to achieve because the convective overpasses over a disdrometer usually last for a few minutes. The lack of large spatial coverage and continuous CR observation can be complemented by satellite remote sensing. However, the uncertainties of satellite-retrieved precipitation properties (e.g., precipitation type

and intensity) remain large especially for the optically thick clouds (Stenz et al., 2014, 2016) because the passive satellite retrievals are more or less representative of cloud top properties, not entire column information.

For the purpose of data compression, the disdrometer-measured DSDs are believed to follow certain distribution functions whose characteristics can be depicted by two or three parameters. Inspired by the work conducted by Marshall and Palmer (1948), the representation of DSD is commonly assumed to follow an exponential function with the simplification of constant intercept (N_{0E} = 0.08 cm^{-4} for straitiform rain). Based on this assumption, the Marshall-Palmer *Z-R* relationship ($Z = 200R^{1.6}$, where Z_e has the unit of mm^6/m^3 and R is in mm/hr) was developed, which directly converts the radar reflectivity at the lowest observed height (the 6th moment of DSD) to surface rain rate (3.5th moment of DSD).

Following the same assumption, a series of *Z-R* relationships targeting different precipitation types were developed based on surface rain rate measurements and near-surface radar reflectivity (e.g., $Z = 300R^{1.4}$ for convective rainfall by Doviak & Zrnic, 1984; $Z = 250R^{1.2}$ for tropical rainfall by Rosenfeld et al., 1993). However, previous studies (e.g., Amitai, 2000; Klazura et al., 1999) have demonstrated that the radar-based precipitation estimates using the default CR *Z-R* relationship in operational National Severe Storms Laboratory precipitation product (Zhang et al., 2011, 2016) are always greater than the direct rain gauge measurements. In order to mitigate the overestimation of CR rain rate from the *Z-R* relationship, the convective rain rate is capped at 103.8 mm/hr in the recent operational NEXRAD-based national precipitation product, Multi-Radar-Multi-Sensor Quantitative Precipitation Estimation (QPE) system (Zhang et al., 2016). This cap also considers the potential contamination of hail that enlarges Z_e observations but contributes nothing to precipitation.

In addition to the existing *Z-R* relationships, the dual-polarization radar products (differential reflectivity, specific differential phase, specific attenuation, etc.) are also related to rain rate estimation (e.g., $R = aA_H^b$, where A_H is the specific attenuation (Diederich et al., 2015; Giangrande et al., 2014; Ryzhkov et al., 2014) and a and b are the coefficient and exponent, respectively). Moreover, the availability of multiple radar variables as well as multiple wavelength radar observations makes the more complicated DSD assumption possible. For example, the normalized Gamma function has been widely applied to active remote sensing precipitation retrieval (e.g., TRMM), especially the dual-frequency precipitation radars onboard the Global Precipitation Measurement (GPM) core observatory. Nonetheless, neither the data sets of dual-polarization nor dual-frequency radar observations are fully developed, thus the operational QPE over the continental United States is still based on power-law *Z-R* relationships with an assumption of exponential DSD (Zhang et al., 2016).

In order to mitigate the overestimation issue presented by the default CR *Z-R* relationship, numerous efforts have been made on calibrating radar-based rainfall estimates with gauge measurements (e.g., Fulton et al., 1998; Haberlandt, 2007; Hossain et al., 2004; Kalinga & Gan, 2006; Xin et al., 1997), and newly developed *Z-R* relationships have been proven to be more accurate for CR rain rate estimate. For example, $Z = 250R^{1.2}$ (Xin et al., 1997) is reported with optimal performance for fast moving convective storms. Using a fixed exponent of 1.4, Amitai (2000) found that CR samples at different locations and time periods feature varying coefficients. Although different CR *Z-R* relationships are provided from previous studies, the application of those relationships is greatly constrained because they were generated from different cases where there are extensively spatial and temporal variations in CR (Chiang et al., 2007; Xiao & Chandrasekar, 1997). That is, no unique set of *Z-R* relationships based on empirical fitting can provide an adequate CR rain rate estimate under a broad range of situations (Trafalis et al., 2002). As mentioned above, the early practice of CR *Z-R* relationship development was built upon the assumption of constant N_{0E} in a power-law form. The intrinsic limitation as revealed in previous studies indicates that constant N_{0E} may not be a valid assumption, and the optimal CR *Z-R* relationship should be developed from disdrometer-measured DSDs.

By combining aircraft in situ measurements and surface disdrometer measurements, the microphysical properties of ice and liquid layers of the SR region were thoroughly studied in previous companion papers (Tian et al., 2016; Wang et al., 2015, 2016). In Part I of this series (Wang et al., 2016), a new SR *Z-R* relationship was developed based on aircraft measured DSD by incorporating the dependence between exponential parameters, and the retrieved rain rates demonstrated better agreement with direct rain gauge measurements than the ones using traditional power law *Z-R* relationship. Although the traditional constant N_{0E}

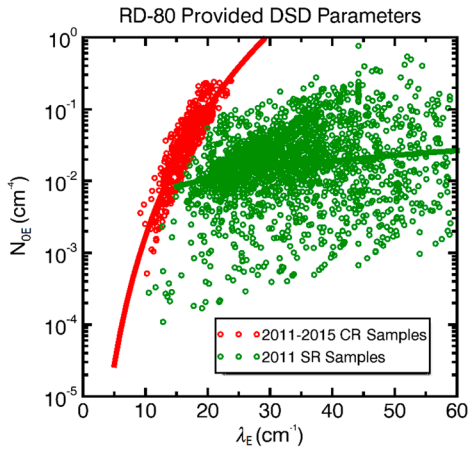

Figure 1. Exponentially fitted intercept parameter (N_{0E}) as a function of slope parameter (λ_E) for the convective rain samples (red dots, 2011–2015) and the stratiform samples (green dots, 2011) collected by the RD-80 disdrometer at the Southern Great Plains central facility. DSD = raindrop size distribution; CR = convective rain; SR = stratiform rain.

assumption seems valid for the SR estimation in Part 1, it could be problematic for the CR estimation as demonstrated in Figure 1, which is the main focus of Part 2 in this study. However, due to the lack of aircraft in situ measurements over the CR region, the surface disdrometer is the sole data source for accurate CR DSD measurements. Given the fact that the operational CR *Z-R* relationship yields severe overestimation compared to rain gauge measurements (e.g., Fulton et al., 1998; Xin et al., 1997), the improvement in CR rain rate estimation is necessary. With the focus of accurate retrieval on CR rain rate from NEXRAD radar reflectivity, instead of constant N_{0E} assumption, this study proposes an alternative approach to parameterize the CR DSD by using the densely distributed surface DSD measurements during the Midlatitude Continental Convective Clouds Experiment (MC3E; Jensen et al., 2015).

2. Data

The distinction in DSD between SR and CR is well known for the phenomenon called N_0 *jump* (Waldvogel, 1974), which reveals the discontinuity in the change of exponentially fitted intercept parameter (N_{0E}) with convective activity from no convection (SR-dominated precipitation corresponds to lower constant N_{0E} values) to convection (CR-dominated precipitation corresponds to higher-varying N_{0E} values). This feature was also captured by the Distromet model RD-80 disdrometer deployed at the Department of Energy (DOE) Atmospheric Radiation Measurement (ARM) Southern Great Plains central facility (SGP, 36°36′18″N, 97°29′6″W). The RD-80 disdrometer transforms the impact of a raindrop falling on the pressure sensor into drop diameter, which has a measurable size range from 0.3 to 5.4 mm (Joss & Waldvogel, 1967, 1969; Kinnel, 1976).

The separation of CR versus SR can be easily achieved by using the hybrid Convective-Stratiform-Anvil (CSA) cloud classification algorithm (Feng et al., 2011) with the input of 5-min 3-D NEXRAD mosaic (Zhang et al., 2011). In this unsupervised cloud classification method, the convective core portion (CC, corresponding to the precipitation type of CR) must have maximum reflectivities exceeding 45 dBZ with contiguous echo top above 6 km, while the SR portion features weak horizontal reflectivity gradient. Notice that there is a possible spatial mismatch between the disdrometer-based point measurement (sampling area of 50 cm^2) and the NEXRAD-based CSA product (1 km^2), that is, the disdrometer could potentially observe non-CR samples within the CSA-defined CR grid. The subgrid variability at the radar pixel scale was quantified by Jaffrain and Berne (2012). In their experiment, a dense network of disdrometers was deployed in a grid area of 1 km × 1 km, and the resulting variation in rain rate estimation fell between −2% to 15%. Therefore, it is a valid approximation to apply the NEXRAD-based classified CR and SR regions to the disdrometer-based point measurement although subgrid inhomogeneity exists.

Figure 1 presents 1 year of SR (8,450 valid samples) and 5 years of CR (794 valid samples) collected by the RD-80 disdrometer at the ARM SGP central facility. These samples have been classified by the hybrid CSA algorithm (Feng et al., 2011) and shown in the form of an exponentially fitted intercept parameter (N_{0E}) as a function of slope parameter (λ_E). Figure 1 also demonstrates that there are no overlaps between the CR and SR samples and exhibits similar normalized variations (defined as the standard deviation divided by the absolute value of mean) in N_{0E} (31.8% for CR and 31.5% for SR, calculated in logarithmic scale) with large differences in λ_E (15.8% for CR and 29.5% for SR). Figure 1, together with the well-known N_0 jump issue, has demonstrated that there is an intrinsic distinction in DSD between SR and CR, and the constant λ_E seems to be a better assumption for the CR.

Although the long-term RD-80 DSD measurements can serve as an indicator revealing the distinction between SR and CR, the investigation of CR DSD cannot be based on RD-80 measurements due to its limited size range. Its maximum measurable raindrop size (5.4 mm) is very close to the upper limit of SR raindrop size (4 mm; Seto & Iguchi, 2015; Wang et al., 2016), thus unsampled large particles are excluded from the RD-80 measurements. Compared to the traditional disdrometer measurements which base on a pressure

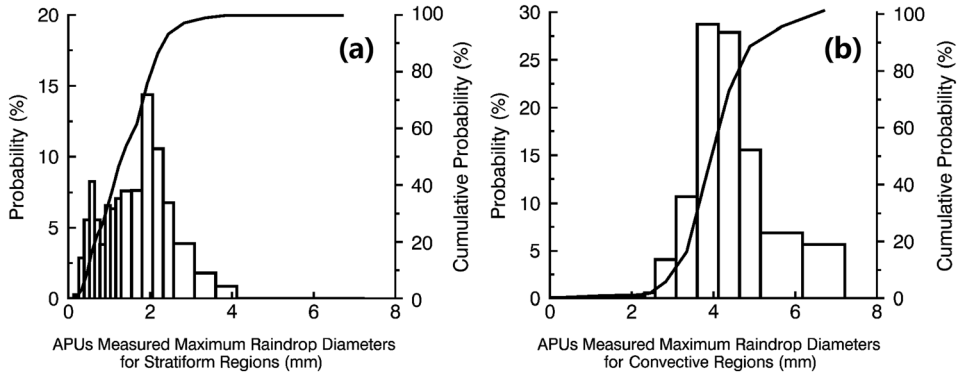

Figure 2. Probability and cumulative probability of maximum raindrop diameter measured by the 17 APUs during MC3E for (a) stratiform rain and (b) convective rain. APUs = Automatic Parsivel Units; MC3E = Midlatitude Continental Convective Clouds Experiment.

transducer, the OTT Automatic Parsivel Units (APUs) employ more advanced laser optical technology and extend the maximum measureable particle size up to 24.5 mm (Brawn & Upton, 2008; Kathiravelu et al., 2016). Figure 2 compares the probabilities and cumulative probabilities of the 17 APUs measured maximum raindrop volume equivalent diameter between SR (a total of 34,518 1-min samples) and CR (a total of 1,226 1-min samples) during the MC3E field campaign. As shown in Figure 2a no SR samples exceed the 4-mm threshold, whereas ~40% CR samples have drop size greater than 4 mm, which is consistent with previous observations from the CC region (e.g., Cao & Zhang, 2009). Although only deployed during the field campaign for a short period, the APUs are chosen as the reliable measurements for CR, which have been used to develop a new CR DSD parameterization in this study.

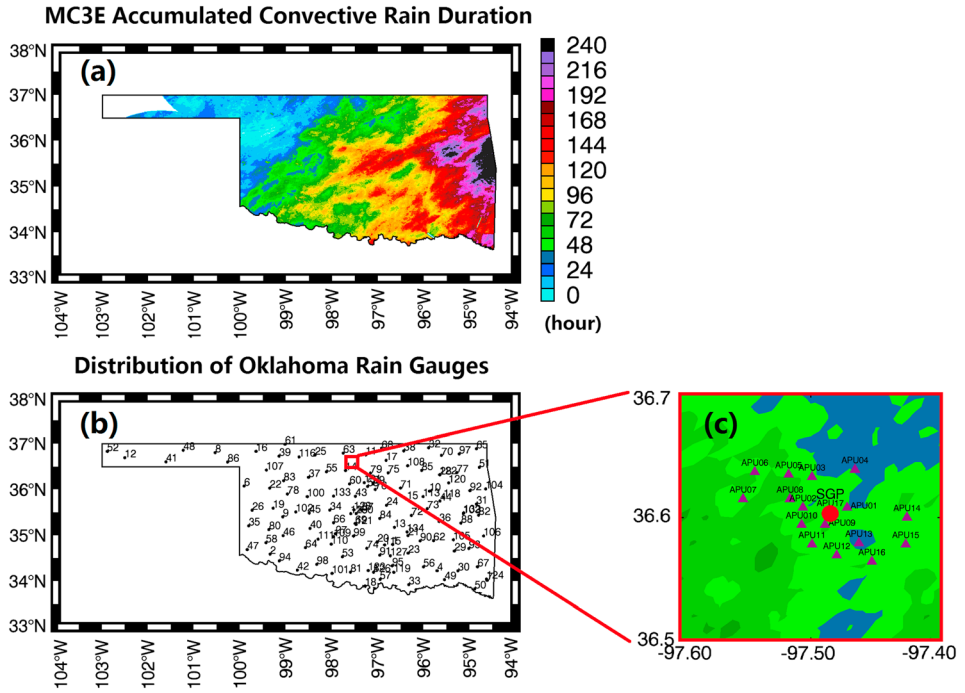

Figure 3. (a) The accumulated convective rain duration during MC3E and the distributions of (b) Mesonet rain gauges and (c) disdrometers (APUs are shown as purple triangles, and RD-80 at the ARM SGP central facility is shown as the red dot) overlaid on convective rain duration. MC3E = Midlatitude Continental Convective Clouds Experiment; APUs = Automatic Parsivel Units; ARM = Atmospheric Radiation Measurement; SGP = Southern Great Plains.

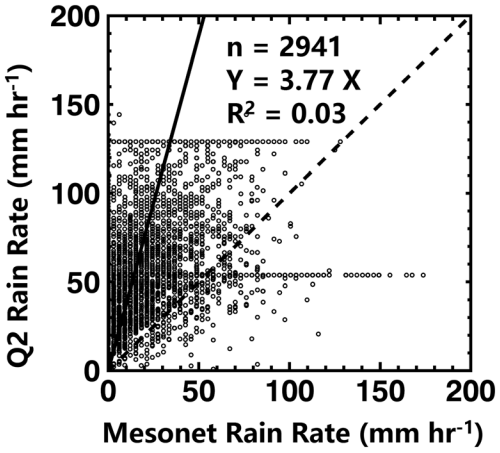

Figure 4. Rain rate comparison between Mesonet rain rate and collocated Q2 rain rate estimates for all collocated convective rain samples.

As a joint field campaign supported by the National Aeronautics and Space Administration GPM Ground Validation program, and the DOE program, MC3E was conducted in north central Oklahoma during the period of April to June 2011. Focusing on improving the understanding and representation of cloud and precipitation properties and their interactions, an unprecedented combination of multiplatform observations was deployed around the ARM SGP site, including aircrafts, ground-based cloud/precipitation radars, as well as an extensive radiosonde array. A focused effort was also made to collect, process, and analyze precipitation measurements during MC3E. As shown in Figure 3a, following the CSA classification, the entire state of Oklahoma experienced more than 70 hr (domain average) of CC overpasses during the 2-month campaign, which were effectively recorded by the dense Mesonet tipping-bucket rain gauge network (Figure 3b, 127 stations, https://www.arm.gov/capabilities/instruments/okm; Atmospheric Radiation Measurement (ARM) Climate Research Facility, 1994). Moreover, as shown in Figure 3c and discussed above, one Disdromet model RD-80 disdrometer and 17 APUs were deployed around the ARM SGP central facility for raindrop size distribution measurements, and more than 20 hr of valid CR samples were collected. Detailed information of those surface instruments can be found in Wang et al. (2016).

As an important data product derived from NEXRAD 3-D mosaic, the National Mosaic and Multi-Sensor Quantitative Precipitation Estimates (Chen et al., 2013; Zhang et al., 2011) can be generated by applying appropriate *Z-R* relationships (Zhang et al., 2011) to the radar reflectivity at the lowest observed height. Specifically for the CR estimation, the default *Z-R* relationship is $Z = 300R^{1.4}$. For the examination of the operational CR rain rate estimate, the CSA algorithm is applied to the locations of 127 Mesonet stations. The classified CC samples (corresponding to the precipitation type of CR) are extracted, and their corresponding Q2 QPEs are compared with direct Mesonet rain rate measurements (Figure 4). As mentioned earlier, the spatial mismatch between point measurements and gridded radar-based QPEs (1 km spatial resolution) is only associated with very limited subgrid variability, thus the Q2 QPEs are comparable with Mesonet rain rate measurements.

Before moving on to the new CR parameterization, it is necessary to match the measurements from different instruments with different sampling rates. In this study, the 1-min APU measurements are resampled with each 5-min NEXRAD interval to match the Q2 retrievals and Mesonet rain rate measurements. After matching the temporal resolution, another question arises: how can we correctly identify the CR samples from different measurements? Although the discrimination between CR and SR can be easily achieved by using their distinct DSD characteristics revealed in previous studies (e.g., Bringi et al., 2003; Caracciolo et al., 2006; Thurai et al., 2016), those classification methods cannot be directly applied to the vast area without DSD measurements. As a result, for the operational purpose of improving CR estimation, CR samples should be identified through the cloud classification algorithm based on radar reflectivity (e.g., CSA), rather than the characteristics of DSD. However, APU radar reflectivity, on average, is 20% larger than NEXRAD reflectivity (Figure 5), thus the radar-based CSA classification with the input of the APU overestimated reflectivity may include some non-CR samples (CC is defined by reflectivity ≥45 dBZ). Moreover, these differences could also result from vertical variability between the lowest radar observation and the ground, as multiple processes can take place (e.g., breakup and coalescence). A sensitivity test has shown that the CSA-classified CR samples have a minimum rain rate value of 4.6 mm/hr measured by the APUs, which apparently belongs to the precipitation type of SR. Therefore, to ensure the robustness of CR DSD statistics, the rainfall rate criterion (Giangrande et al., 2014; Nzeukou et al.,

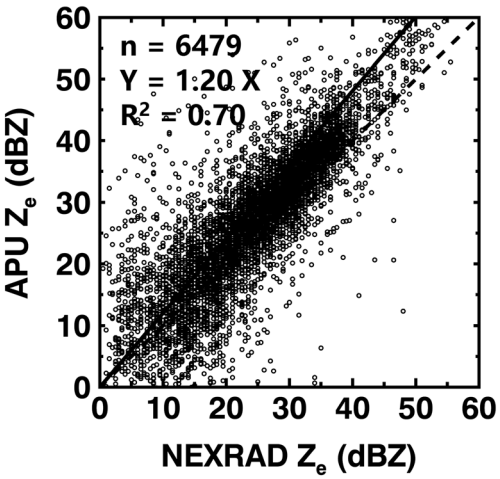

Figure 5. Comparison of radar reflectivity (Z_e) between NEXRAD observations and collocated APU calculations. NEXRAD = Next-Generation Radar; APU = Automatic Parsivel Unit.

Table 1
The Shape-Corrected Raindrop Volume-Equivalent Diameter Classification for the APU

Channel number	Average diameter (mm)
1	0.064
2	0.193
3	0.321
4	0.450
5	0.579
6	0.708
7	0.836
8	0.965
9	1.094
10	1.223
11	1.416
12	1.674
13	1.931
14	2.189
15	2.446
16	2.832
17	3.347
18	3.862
19	4.378
20	4.892
21	5.665
22	6.695
23	7.725
24	8.755
25	9.785
26	11.330
27	13.390
28	15.450
29	17.510
30	19.570
31	22.145
32	25.235

2004; Tokay & Short, 1996) method is introduced for the identification of CR overpasses over the APU stations in this study, which simply assumes all rain rates ≥10 mm/hr as CR samples

As shown in Figure 4, on average, CR rain rate estimates from Q2 based on the power-law relationship of $Z = 300R^{1.4}$ are almost fourfold the collocated Mesonet rain rate measurements with a low correlation coefficient. It is well known that tipping buckets suffer from nonnegligible underestimation issues due to the undercatch of rain drops during tipping (Duchon et al., 2014; Parsons, 1941). Previous studies (e.g., Colli et al., 2013; Duchon & Biddle, 2010) have shown that the water loss can be enhanced by horizontal wind, which is usually associated with convective overpasses. However, even for CR rain rates greater than 200 mm/hr, the underestimation of tipping bucket measurements caused by water loss is believed to be about 10–15% (Molini et al., 2005), which can only account for a very limited portion of the large discrepancy between direct measurements and radar retrievals. As a result, the tipping bucket correction is not performed in this study, and the focus is put on the improvement of radar-based rain rate estimation.

Using the rainfall rate criterion method, a total of 238 5-min CR samples have been collected from 17 APUs during MC3E. As above mentioned, the theoretical design of the APU can measure raindrop sizes up to 25 mm, which is unrealistically large even for CR. The maximum valid measured raindrop size is 9.18 mm (Adirosi et al., 2016) based on the statistical results from all available GPM Ground Validation field campaigns related to warm season convection, including the Hydrological Cycle in the Mediterranean Experiment (2012; Ferretti et al., 2014), the Iowa Flood Studies (2013; https://pmm.nasa.gov/ifloods), and the Integrated Precipitation and Hydrology Experiment (2015; https://pmm.nasa.gov/IPHEx). Moreover, as clarified in the APU user manual, the first two channels (average particle size of 0.064 and 0.193 mm) lack evaluation because they are outside the measurement range (https://www.esrl.noaa.gov/psd/data/obs/instruments/OpticalDisdrometer.pdf). Thus, this study constrains the APU-measured DSD spectrum to 23 size channels ranging from 0.321 to 9.785 mm based on the shape-corrected (Beard, 1976) volume-equivalent diameter (ftp://ghrc.nsstc.nasa.gov/pub/doc/gpmgv/parsivel/DataFormat_parsivel_fieldCampaign.pdf). Detailed APU DSD spectrum information is listed in Table 1. The CR DSD fits using Exponential and Gamma functions (Ulbrich, 1983) are carried out accordingly, employing the same algorithm used in SR region (McFarquhar et al., 2007; Press et al., 1992; Wang et al., 2016) as follows (in centimeter-gram-second units):

$$N(D) = N_{0E}e^{-\lambda_E D}, \tag{1}$$

$$N(D) = N_{0\Gamma}D^{\mu_\Gamma}e^{-\lambda_\Gamma D}. \tag{2}$$

The fitted results are discussed in section 3.

3. Results

3.1. Sensitivity of Fitting Spectrum Subset to the Precipitation Estimation

As suggested by McFarquhar and List (1993), the fitted DSD spectra are very sensitive to the manners of fitting. Conventionally, almost all the DSD fitting practices take into account all available measured raindrops starting from the minimum to the maximum detectable sizes (e.g., Bringi et al., 2002, 2003; Gorgucci et al., 2002; Zhang et al., 2001, 2003). Note that the variability of DSD fitting is greatly determined by small raindrops (featuring orders of magnitude higher in droplet number concentration than larger raindrops). In order to overcome the uncertainty caused by small raindrops, higher moments of DSD representation (e.g., Kozu &

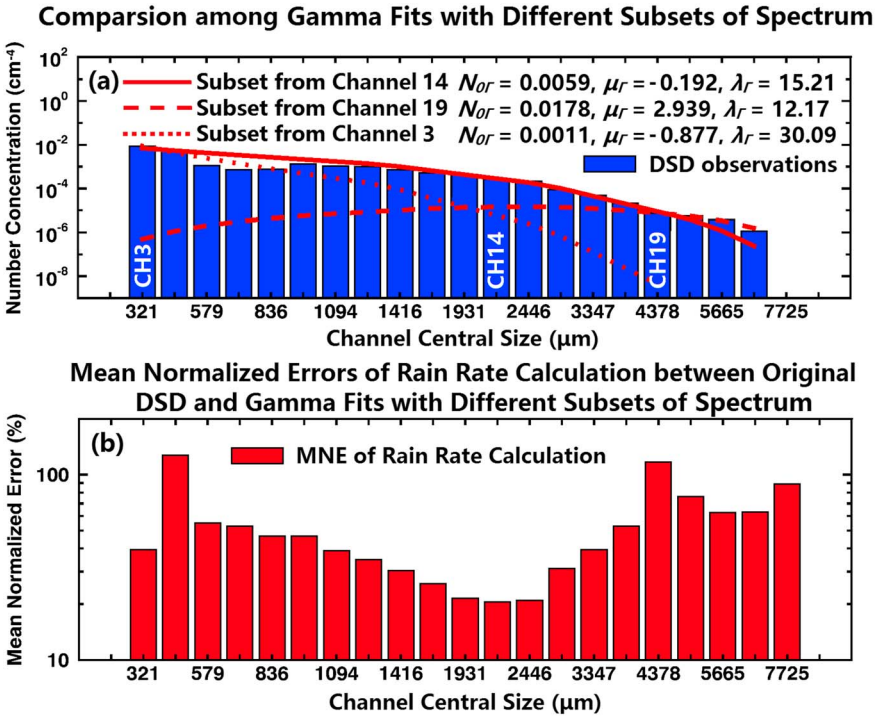

Figure 6. (a) Gamma fitted raindrop size distribution (DSDs) using three different subsets of the DSD spectrum. (b) Comparison of mean normalized errors between rain rates calculated from the Automatic Parsivel Unit-observed DSDs and gamma fitted DSDs with respect to different subsets of DSD spectrum. MNE = mean normalized error.

Nakamura, 1991; Ulbrich & Atlas, 1998; Vivekanandan et al., 2004) are introduced into the DSD fitting to balance the contribution of larger raindrops, and the *n*th moment is calculated as follows:

$$M(n) = \int_{D_{\min}}^{D_{\max}} N(D) D^n \mathrm{d}D, \tag{3}$$

where $D_{\min}$ and $D_{\max}$ are the minimum and maximum raindrops, liquid water content is proportional to *M(3)*, rain rate is approximately represented by *M(3.5)*, and *M(6)* is for Z_e. Different combinations of moments are investigated for the best fitting of DSD (e.g., Kozu & Nakamura, 1991; Testud et al., 2001; Zhang et al., 2001). The representation of DSD containing large raindrops is still not optimal due to the relatively larger errors in higher moment measurements (for example, the inconsistent collocated Z_e values shown in Figure 5).

As revealed in previous studies (e.g., Chen et al., 2017; Tokay et al., 2013), APUs tend to severely underestimate the number of small particles especially for heavy precipitation. With the focus of accurate retrieval on CR rain rate, instead of using the multimoment fit of DSD, this study proposes an alternative approach of only utilizing the APU measured rain rate as a constraint to evaluate the zeroth moment fit of the DSD. In order to examine the small raindrops' impact on the rain rate calculation, DSD fitting based on different subsets of the DSD spectrum (changing the $D_{\min}$ in fitting) has been performed in this study. Figure 6a demonstrates an example of Gamma fitted results using three different subsets of the spectrum (APU03 at 10:20 UTC). The fitted curve (red dotted line) starting from APU channel 3 conforms to the observed DSDs (blue bars) at the first few channels but soon suffers from severe underestimation in number concentration toward the end of the spectrum. On the contrary, the red dashed line starting from APU channel 19 has excellent agreement for the last few channels but with severe underestimation in number concentration in the smaller size channels.

For the quantification of different DSD subsets' impact on rain rate calculation, subset analysis starting from each channel is performed on all CR DSD samples, and their mean normalized errors (MNEs) are shown in Figure 6b which is defined as follows:

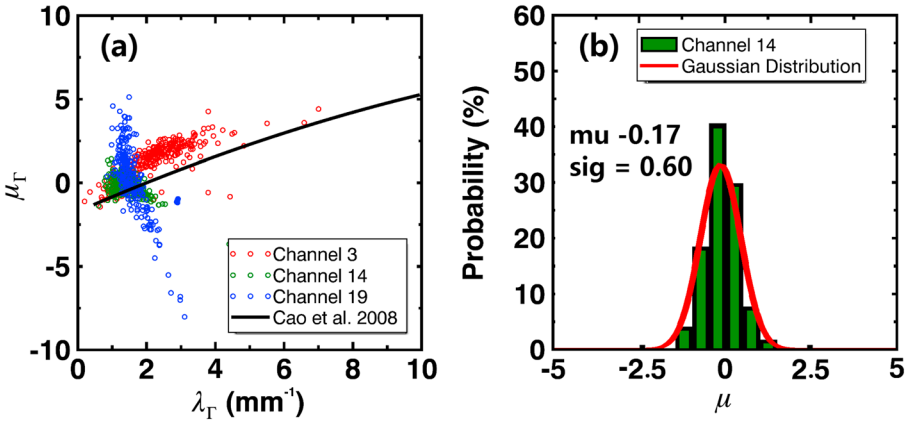

Figure 7. (a) Comparison of the μ_Γ-λ_Γ relationships between three different subsets of spectrum from this study and from Cao et al. (2008). (b) Probability distributions of μ_Γ from the subsetting scheme of channel 14 and Gaussian.

$$MNE = \frac{1}{n}\sum_{i=1}^{n}\frac{|R_{\text{measure}} - R_{\text{calc}}|}{R_{\text{measure}}}, \tag{4}$$

where R_{measure} is the rain rate measured by APUs and R_{calc} is calculated using the fitted DSD based on the following equation:

$$RR\left(\frac{\text{mm}}{\text{hr}}\right) = 3.6\times10^{6}\int_{D_{\min}}^{D_{\max}} N_{0E}e^{-\lambda_E D}\frac{\pi}{6}D^3V(D)\text{d}D. \tag{5}$$

equation (5) uses the assumption of pristine terminal velocity defined by Gunn and Kinzer (1949), which is also used for the removal of spurious APU DSD measurements by default (Jaffrain & Berne, 2011; Tokay et al., 2001). As shown in Figure 6b, the fitted Gamma curve using the subset from channel 14 has the minimal MNE, which is consistent with Figure 6a (red solid line), where the best overall representation of the observed DSD is also found at channel 14.

As revealed in previous studies (e.g., Brandes et al., 2004; Cao et al., 2008; Zhang et al., 2001), the Gamma dispersion (μ_Γ) and slope (λ_Γ) parameters are highly related, which can serve as the constraint for the dual-polarization or dual-frequency DSD retrieval. The relationships between Gamma parameters using three different subsets of the spectrum in Figure 6 are examined, where an interesting clockwise rotation of the fitted μ_Γ-λ_Γ curves is observed as demonstrated in Figure 7a. Channel 3 illustrates large similarities to the classic μ_Γ-λ_Γ curve found by Cao et al. (2008). However, the trend from channel 14 subset follows a horizontal line, and channel 19 demonstrates a flipped trend compared to those from channel 3. This variation is not only supported by the three selected subsets of spectrum, smooth transition in rotation angle is also observed by using the continuous increment in subset channels (not shown). For convective precipitation featuring large raindrops, this study proposes an alternative approach to reduce the uncertainty associated with small raindrops by subsetting the spectra in the DSD Gamma fit, and the choice of subset scheme has a tremendous impact on the resulting μ_Γ-λ_Γ relationship.

Although the Gamma size distribution is commonly used in DSD parameterization, the constant dispersion parameter μ_Γ is always assumed in operation for simplification. For instance, μ_Γ = 2 in both TRMM and GPM precipitation radar rain rate retrieval (Kozu et al., 2009), and the surface-observed μ_Γ mode values are believed to be around 4–6 (Illingworth & Blackman, 2002; Kozu & Nakamura, 1991; Tokay & Short, 1996). As shown in Figure 7b, by subsetting from channel 14, the probability distribution of μ_Γ follows the Gaussian distribution with a mean value of −0.17 and standard deviation of 0.60, making the DSD fit using Exponential function a reasonable assumption which is equivalent to set μ_Γ = 0 in Gamma fit. This conclusion is also supported by Zhang et al. (2017), where convective rainfall is found to be more exponentially distributed than SR due to small μ_Γ values. Similar to Figure 6b, Figure 8b examines the sensitivity of the DSD spectrum subset to rain rate calculation using Exponential fitting, where

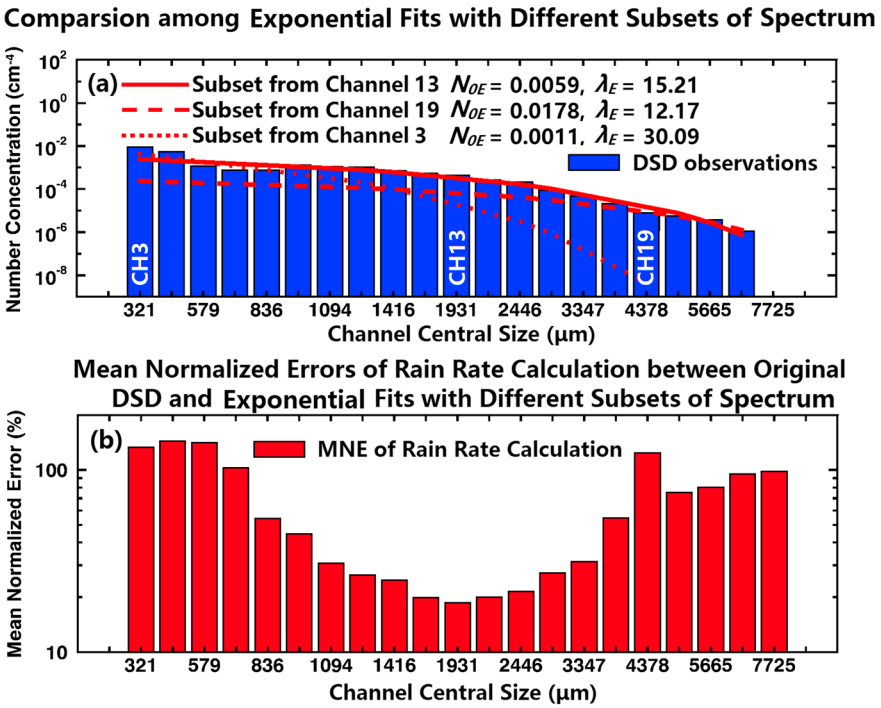

Figure 8. Similar to Figure 6 but using exponential fitting.

the lowest MNE is also found in the middle channels (channel 13 in this study). Moreover, the subset of channel 13 can best represent the observed DSD as shown in Figure 8a.

It is necessary to note that by using different criteria of error evaluation methods (e.g., mean square error, root mean square error, mean absolute error, and correlation coefficient), the optimal channel subset scheme always falls in the middle of the spectrum. The MNE is chosen for the largest contrast among the channels, and the result could vary using different error evaluation approaches.

3.2. Comparison Between Different Parameterization Schemes

Since we have confidence in the subsetting scheme of DSD spectra using Exponential fitting, the next step is to determine the best approach to establish the empirical relationship between the fitted parameters. Figure 9a demonstrates two alternative methods in the curve fitting schemes based on all APU-observed CR samples. One is based on the constant assumption (red solid line, the mean of λ_E values):

$$\lambda_E = 12.2\ \mathrm{cm}^{-1}, \tag{6}$$

along with the others using power law regression (red dashed line):

$$N_{0E} = 3.38\times10^{-8}\lambda_E^{4.75}. \tag{7}$$

By substituting those assumptions into the radar equation:

$$Z_e^*\left(\mathrm{mm}^6/\mathrm{m}^3\right) = 10^{12}\int_0^\infty N_{0E}e^{-\lambda_E D}D^6\mathrm{d}D, \tag{8}$$

the direct relationships between N_{0E} and Z_e can be established as either

$$N_{0E} = \frac{Z_e(\mathrm{mm}^6/\mathrm{m}^3)\times12.2^7}{\Gamma(7)\times10^{12}}, \tag{9}$$

or

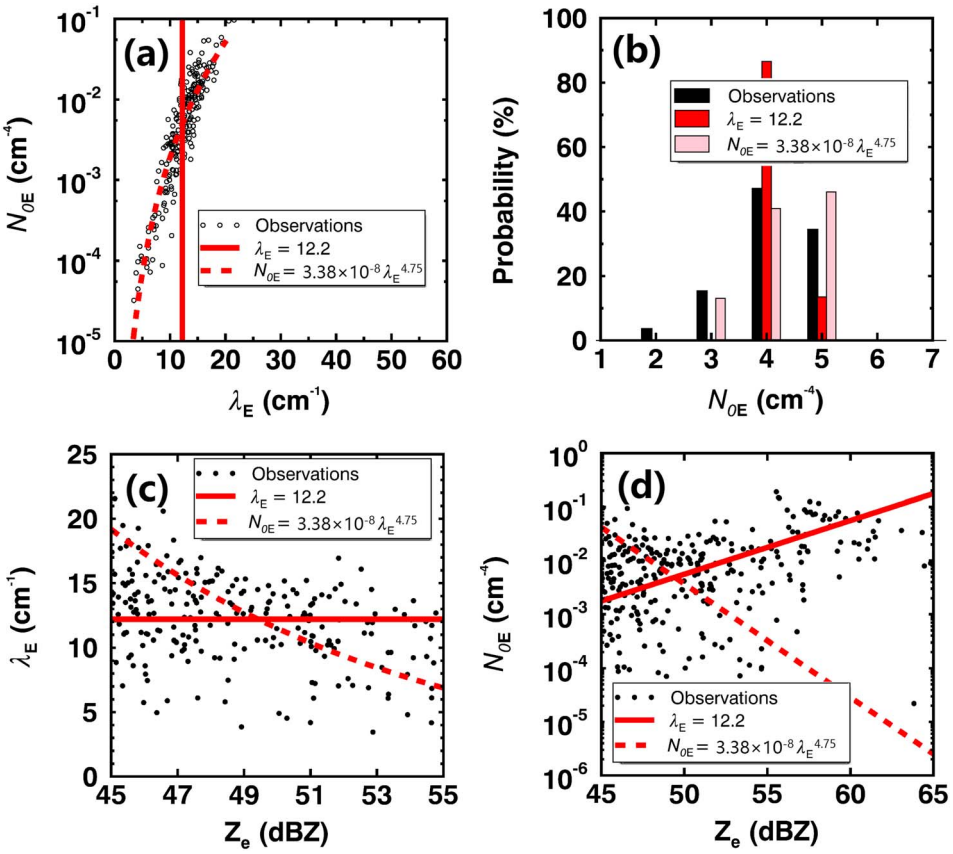

Figure 9. Comparison between (a) constant λ_E assumption and fitted N_{0E}-λ_E relationship, and their applications in (b) N_{0E} distribution, (c) Z_e-λ_E relationship, as well as (d) Z_e-N_{0E} relationship.

$$N_{0E} = 3.38\times10^{-8}\left(\frac{2.4336\times10^{7}}{Z_e(\mathrm{mm^6/m^3})}\right)^{\frac{1}{0.47}}. \tag{10}$$

Although equation (7) outperforms equation (6) in capturing the N_{0E}-λ_E variation as shown in Figure 9a, it also generates a biased N_{0E} distribution (Figure 9b), as well as an incorrect N_{0E} (Figure 9d) variation with the input of the APU calculated Z_e. In Figure 9b, the observed that N_{0E} (black bars) values have the mode of 10^{-2} cm^{-4}, which is well preserved by the constant λ_E assumption (equation (6)), but the peak is skewed to the larger N_{0E} value when using the fitted N_{0E}-λ_E relationship (equation (7)). For the comparison of λ_E-Z_e relationships shown in Figure 9c, no significant difference in λ_E retrieved from Z_e is found based on different approaches. However, the observed increasing trend in the N_{0E}-Z_e relationship is captured by the constant λ_E assumption, whereas it becomes a decreasing trend by using the N_{0E}-λ_E relationship as illustrated in Figure 9d. It is necessary to note that from the original N_0 jump theory, after the drastic increase in N_{0E} from SR to CR, N_{0E} tends to decay with increasing convective activity, which is strongly reflected in the Gamma function fitting. For example, the relationship $N_{0\Gamma} = 4\times10^{8}\,R^{-4.3}$ was established by Maki et al. (2001) to address this issue.

3.3. Evaluation of the New CR Precipitation Estimation

By substituting equation (9) into the definition of the rain rate (equation (5)), the new CR rain rate can be estimated as follow:

$$RR(\mathrm{mm/hr}) = 3.6\times10^{6}\int_{D_{\min}}^{D_{\max}}\frac{Z_e(\mathrm{mm^6/m^3})\times12.2^{7}}{\Gamma(7)\times10^{12}}e^{-12.2D}\frac{\pi}{6}D^{3}V(D)\mathrm{d}D, \tag{11}$$

where the terminal velocity $V(D)$ still follows the pristine assumption by Gunn and Kinzer (1949).

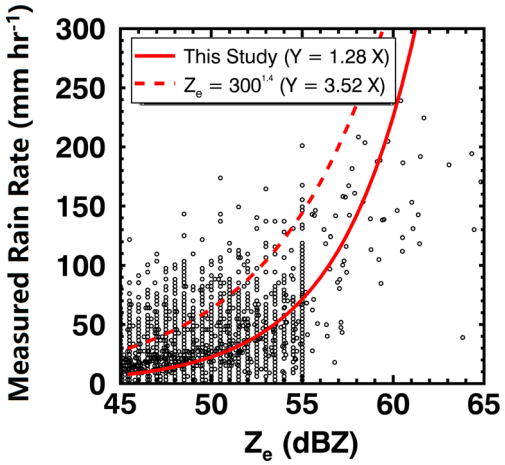

Figure 10. The scatter plot of measured rain rates (Mesonet and APUs) versus their collocated lowest available Z_e (NEXRAD observed and APU calculated) during MC3E, overlain by the newly developed *Z-R* relationship (red solid line) and the traditional *Z-R* relationship (red dash line). NEXRAD = Next-Generation Radar; APU = Automatic Parsivel Unit; MC3E = Midlatitude Continental Convective Clouds Experiment.

To evaluate the performance of the newly developed *Z-R* relationship, in addition to the 17 APU disdrometers measurements, an independent data set of CR rain rate measurements by 127 Mesonet rain gauges and their collocated radar reflectivity at the lowest observed height during MC3E (2941 valid samples, classified by CSA) are also examined in Figure 10. The newly developed relationship provides a more reasonable rain rate estimation, compared to the traditional power law CR *Z-R* relationship, which indicates that the constant λ_E could potentially be a better assumption instead of a constant N_{0E} for CR rain rate estimation.

Although lower CR rain rates are generated using the newly developed *Z-R* relationship, many critical issues are either overlooked or oversimplified in this study. For instance, the deformation of large raindrops is not fully considered. As shown in Figures 11a and 11b, the CSA classified CC regions (red color) all correspond to high differential reflectivity (Z_{DR}, defined as the difference between the horizontal and vertical reflectivity factors) values greater than 2 dB, indicating that the observed raindrops are highly deformed with lower axis ratios (McFarquhar & Heymsfield, 1996). In contrast, the vast SR regions feature much lower Z_{DR}, where spherical raindrop assumption can work better. Moreover, the *V(D)* follows the pristine assumption developed by Gunn and Kinzer (1949) for stagnant air, in which the impacts of vertical air motion and particle deformation are overlooked. In recent studies, more sophisticated approximations in raindrop fall velocity are developed in the forms of polynomial (e.g., Brandes et al., 2008; Cao et al., 2008), power law (e.g., Atlas & Ulbrich, 1977; Pei et al., 2014), and exponential (e.g., Atlas et al., 1973). However, no matter which mathematical form the *V*(*D*) is, or to which order the polynomial is truncated, one fixed *V*(*D*) relationship cannot fully account for the interactions among complex mechanisms (e.g., coalescence, breakup, turbulence, and winds) during precipitation events. Thus, synthetic consideration and parameterization of those processes are necessary for accurately estimating CR rain rate. Among the environmental variables, the vertical air motion plays an important role as it has immediate impact on the raindrop fall velocity. Traditionally, the quantification of vertical air motion is difficult to achieve because it can vary drastically within small temporal and spatial scales, especially within the CR region. In a recent study conducted by North et al. (2017), the vertical air motion is successfully retrieved for deep convective clouds based on the ARM scanning radar, which may shed light on the future investigation of CR rain rate.

Figure 11c attempts to summarize the relationships among the three simplified variables relevant to the best estimate of CR rain rate. First, large deformed raindrops have drag effects on the ambient air, which is in the opposite direction to the CR updraft. Meanwhile, stronger updrafts enhance the raindrop deformation. Second, large raindrops exhibit faster fall velocities, which is directly related to raindrop deformation. However, when deformation happens, raindrops expose more contact area to the updraft which slows down the velocity of the falling raindrop. Lastly, the fall velocity and updraft are negatively related as they are in opposing directions. Nonetheless, all three factors indicate higher rain rates, so the robust estimation of CR

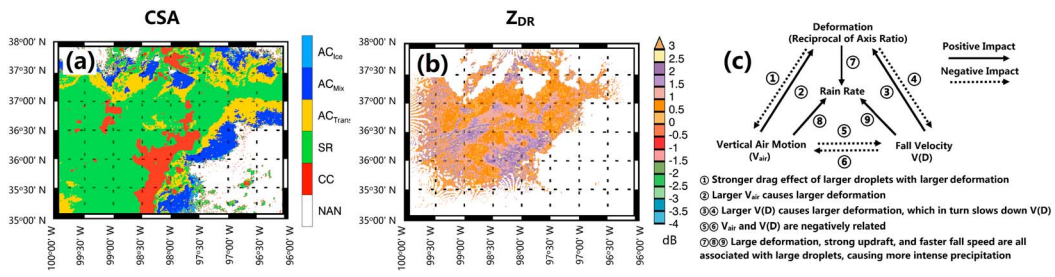

Figure 11. The example of (a) CSA classification based on 3-D radar reflectivity and (b) the observed near-surface differential reflectivity (Z_{DR}) from single radar observation sampled on 20 May 2011 09:05 UTC, and (c) the conceptual relationships between environmental variables and rain rate retrieval. CSA = Convective-Stratiform-Anvil.

rain rate can only be based on an in-depth understanding of those relationships with more observations. In addition to these three factors, multiple transition processes from cloud to precipitation (e.g., Kumjian & Prat, 2014; Fan et al., 2015, 2018; McFarquhar, 2004a, 2004b; Pruppacher & Klett, 1996), including collision-coalescence, breakup, and evaporation, also play important roles in CR precipitation estimation, which warrant further joint investigation.

4. Summary and Conclusions

In this study, a total of 20 hr of CR DSD samples measured by 17 APU disdrometers during MC3E were collected and processed to investigate the CR precipitation properties. The surface in situ measurements were carefully processed and examined, and an alternative CR DSD parameterization scheme was developed, which was further applied to the CR rain rate estimation. The main conclusions can be summarized as follows:

1. Compared to the SR DSD, two distinctive features of the CR DSD are observed based on a large amount of disdrometer DSD measurements over the SGP region. They are (a) broader spectrum distribution (maximum raindrop size can be up to 8 mm versus less than 4 mm in SR) and (b) less variation in λ_E (15.8% for CR versus 29.5% for SR). The constant N_{0E} assumption is valid for the SR estimation but may be problematic for the CR estimation. The assumption of constant λ_E is more capable in capturing the natural N_{0E}-λ_E variation observed by the APUs. By applying $\lambda_E = 12.2\ \text{cm}^{-1}$ to the definitions of radar reflectivity factor, CR rain rates can be directly retrieved from the observed Z_e values.
2. Since the fitted DSD spectra are sensitive to the manners of fitting, we propose an alternative approach to reduce the uncertainty associated with small raindrops by introducing higher moments of DSD representation in the DSD fitting in this study. For the CR DSD, both the Gamma and Exponential DSD function fits demonstrate a large sensitivity to spectra subsetting schemes. As the starting channel of the DSD is shifted toward the larger raindrop sizes, an interesting clockwise rotation in the $N_{0\Gamma}$-λ_Γ curves is observed, where the curve of default full spectra fitting resembles to the classic $N_{0\Gamma}$-λ_Γ relationship. However, with the measured rain rate as a constraint, the best representation of CR DSD is found by subsetting from the middle of the spectra, where μ_Γ is close to 0, making the DSD fit using Exponential function a reasonable assumption.
3. To evaluate the performance of the newly developed *Z-R* relationship, in addition to the 17 APU disdrometer measurements, an independent data set of CR rain rate measurements by 127 Mesonet rain gauges and their collocated radar reflectivity at the lowest observed height during MC3E are also examined. Compared to the severe overestimation using the traditional power law CR *Z-R* relationship ($Z = 300\ R^{1.4}$), the newly estimated rain rate is more reasonable and close to the direct CR rain rate measurements.

Although many critical factors related to CR rain rate estimation are overlooked or over-simplified, and the conclusion was merely based on intensive observations during one field campaign, this study attempts to explore an alternative approach of CR DSD parameterization. By changing to the assumption of constant λ_E, the overestimation issue in CR rain rate calculation is greatly mitigated. It is worthwhile to note that the new *Z-R* relationship was established for the MC3E campaign, and the adjustments of optimal subsetting spectra, as well as the choice of constant λ_E could vary for different climatic regions by different observations. For CR precipitation estimation, the calculated rain rate could also be impacted by choosing different *V(D)* relationships.

Acknowledgments
The data were obtained from the Atmospheric Radiation Measurement (ARM) Program sponsored by the U.S. Department of Energy (DOE) Office of Energy Research, Office of Health and Environmental Research, and Environmental Sciences Division. This study was primarily supported by DOE CMDV project at University of Arizona with award DE-SC0017015 and the NOAA R2O project at University of North Dakota project under grant NA15NWS4680004. The disdrometer in situ measurements during MC3E are available at the U.S. Department of Energy ARM data archive (http://www.archive.arm.gov/armlogin/login.jsp). We would like to thank Timothy Logan for proofreading the manuscript.

References

Adirosi, E., Volpi, E., Lombardo, F., & Baldini, L. (2016). Raindrop size distribution: Fitting performance of common theoretical models. *Advances in Water Resources*, *96*, 290–305. https://doi.org/10.1016/j.advwatres.2016.07.010

Amitai, E. (2000). Systematic variation of observed radar reflectivity–rainfall rate relations in the tropics. *Journal of Applied Meteorology*, *39*(12), 2198–2208. https://doi.org/10.1175/1520-0450(2001)040<2198:SVOORR>2.0.CO;2

Ashley, W. S., Mote, T. L., Dixon, P. G., Trotter, S. L., Powell, E. J., Durkee, J. D., & Grundstein, A. J. (2003). Distribution of mesoscale convective complex rainfall in the United States. *Monthly Weather Review*, *131*(12), 3003–3017. https://doi.org/10.1175/1520-0493(2003)131<3003:DOMCCR>2.0.CO;2

Atlas, D., Srivastava, R. C., & Sekhon, R. (1973). Doppler radar characteristics of precipitation at vertical incidence. *Reviews of Geophysics and Space Physics*, *11*(1), 1–35. https://doi.org/10.1029/RG011i001p00001

Atlas, D., & Ulbrich, C. W. (1977). Path- and area-integrated rainfall measurement by microwave attenuation in the 1–3 cm band. *Journal of Applied Meteorology*, *16*(12), 1322–1331. https://doi.org/10.1175/1520-0450(1977)016<1322:PAAIRM>2.0.CO;2

Atmospheric Radiation Measurement (ARM) Climate Research Facility (1994). updated hourly. Oklahoma Mesonet (15OKM). 2011-04-22 to 2011-06-02, Southern Great Plains (SGP). Compiled by L. Gregory. Atmospheric Radiation Measurement (ARM) Climate Research Facility Data Archive: Oak Ridge, Tennessee, USA. Data set accessed 2017-09-10.

Beard, K. V. (1976). Terminal velocity and shape of cloud and precipitation drops aloft. *Journal of the Atmospheric Sciences*, *33*(5), 851–864. https://doi.org/10.1175/1520-0469(1976)033<0851:TVASOC>2.0.CO;2

Brandes, E. A., Ikeda, K., Thompson, G., & Schönhuber, M. (2008). Aggregate terminal velocity/temperature relations. *Journal of Applied Meteorology and Climatology*, *47*(10), 2729–2736. https://doi.org/10.1175/2008JAMC1869.1

Brandes, E. A., Zhang, G., & Vivekanandan, J. (2004). Drop size distribution retrieval with polarimetric radar: Model and application. *Journal of Applied Meteorology*, *43*(3), 461–475. https://doi.org/10.1175/1520-0450(2004)043<0461:DSDRWP>2.0.CO;2

Brawn, D., & Upton, G. (2008). On the measurement of atmospheric gamma drop-size distributions. *Atmospheric Science Letters*, *9*(4), 245–247. https://doi.org/10.1002/asl.198

Bringi, V. N., Chandrasekar, V., Hubbert, J., Gorgucci, E., Randeu, W. L., & Schoenhuber, M. (2003). Raindrop size distribution in different climatic regimes from disdrometer and dual-polarized radar analysis. *Journal of the Atmospheric Sciences*, *60*(2), 354–365. https://doi.org/10.1175/1520-0469(2003)060<0354:RSDIDC>2.0.CO;2

Bringi, V. N., Huang, G., Chandrasekar, V., & Gorgucci, E. (2002). A methodology for estimating the parameters of a gamma raindrop size distribution model from polarimetric radar data: Application to a squall-line event from the TRMM/Brazil campaign. *Journal of Atmospheric and Oceanic Technology*, *19*(5), 633–645. https://doi.org/10.1175/1520-0426(2002)019<0633:AMFETP>2.0.CO;2

Cao, Q., & Zhang, G. (2009). Errors in estimating raindrop size distribution parameters employing disdrometer and simulated raindrop spectra. *Journal of Applied Meteorology and Climatology*, *48*(2), 406–425. https://doi.org/10.1175/2008JAMC2026.1

Cao, Q., Zhang, G., Brandes, E., Schuur, T., Ryzhkov, A., & Ikeda, K. (2008). Analysis of video disdrometer and Polarimetric radar data to characterize rain microphysics in Oklahoma. *Journal of Applied Meteorology and Climatology*, *47*(8), 2238–2255. https://doi.org/10.1175/2008JAMC1732.1

Caracciolo, C., Prodi, F., Battaglia, A., & Porcu, F. (2006). Analysis of the moments and parameters of a gamma DSD to infer precipitation properties. *Atmospheric Research*, *80*, 165–186.

Chen, B., Hu, Z., Liu, L., & Zhang, G. (2017). Raindrop size distribution measurements at 4,500 m on the Tibetan plateau during TIPEX-III. *Journal of Geophysical Research: Atmospheres*, *122*, 11,092–11,106. https://doi.org/10.1002/2017JD027233

Chen, S., Gourley, J. J., Hong, Y., Kirstetter, P. E., Zhang, J., Howard, K., et al. (2013). Evaluation and Uncertainty Estimation of NOAA/NSSL Next-Generation National Mosaic Quantitative Precipitation Estimation Product (Q2) over the Continental United States. *Journal of Hydrometeorology*, *14*, 1308–1322. https://doi.org/10.1175/JHM-D-12-0150.1

Chiang, Y. M., Chang, F. C., Jou, J. D. B., & Lin, P. F. (2007). Dynamic ANN for precipitation estimation and forecasting from radar observations. *Journal of Hydrology*, *334*(1–2), 250–261. https://doi.org/10.1016/j.jhydrol.2006.10.021

Colli, M., Lanza, L., & Chan, P. (2013). Co-located tipping-bucket and optical drop counter RI measurements and a simulated correction algorithm. *Atmospheric Research*, *119*, 3–12. https://doi.org/10.1016/j.atmosres.2011.07.018

Diederich, M., Ryzhkov, A., Simmer, C., Zhang, P., & Trömel, S. (2015). Use of specific attenuation for rainfall measurement at X-band radar wavelengths. Part II: Rainfall estimates and comparison with rain gauges. *Journal of Hydrometeorology*, *16*(2), 503–516. https://doi.org/10.1175/JHM-D-14-0067.1

Doviak, R., & Zrnic, D. (1984). *Doppler radar and weather observations* (p. 458). Cambridge, MA: Academic Press.

Duchon, C., & Biddle, J. (2010). Undercatch of tipping-bucket gauges in high rain rate events. *Advances in Geosciences*, *25*, 11–15. https://doi.org/10.5194/adgeo-25-11-2010

Duchon, C., Fiebrich, C., & Grimsley, D. (2014). Using high-speed photography to study Undercatch in tipping-bucket rain gauges. *Journal of Atmospheric and Oceanic Technology*, *31*(6), 1330–1336. https://doi.org/10.1175/JTECH-D-13-00169.1

Fan, J., Liu, Y. C., Xu, K. M., North, K., Collis, S., Dong, X., et al. (2015). Improving representation of convective transport for scale-aware parameterization: 1. Convection and cloud properties simulated with spectral bin and bulk microphysics. *Journal of Geophysical Research: Atmospheres*, *120*, 3485–3509. https://doi.org/10.1002/2014JD022142

Fan, J., Rosenfeld, D., Zhang, Y., Giangrande, S. E., Li, Z., Machado, L. A. T., et al. (2018). Substantial convection and precipitation enhancements by ultrafine aerosol particles. *Science*, *359*(6374), 411–418. https://doi.org/10.1126/science.aan8461

Feng, Z., Dong, X., Xi, B., McFarlane, S., Kennedy, A., Lin, B., & Minnis, P. (2012). Life cycle of mid-latitude deep convective systems in a Lagrangian framework. *Journal of Geophysical Research*, *117*, D23201. https://doi.org/10.1029/2012JD018362

Feng, Z., Dong, X., Xi, B., Schumacher, C., Minnis, P., & Khaiyer, M. (2011). TOA radiation budget of convective core/stratiform rain and anvils from deep convective systems. *Journal of Geophysical Research*, *116*, D23202. https://doi.org/10.1029/2011JD16451

Ferretti, R., Pichelli, E., Gentile, S., Maiello, I., Cimini, D., Davolio, S., et al. (2014). Overview of the first HyMeX special observation period over Italy: Observations and model results. *Hydrology and Earth System Sciences*, *18*(5), 1953–1977. https://doi.org/10.5194/hess-18-1953-2014.

Fritsch, J. M., Kane, R. J., & Chelius, C. R. (1986). The contribution of mesoscale convective weather systems to the warm-season precipitation in the United States. *Journal of Applied Meteorology and Climatology*, *25*(10), 1333–1345. https://doi.org/10.1175/1520-0450(1986)025<1333:TCOMCW>2.0.CO;2

Fulton, R. A., Breidenbach, J. P., Seo, D., Miller, D. A., & O'Bannon, T. (1998). The WSR-88D rainfall algorithm. *Weather Forecasting*, *13*(2), 377–395. https://doi.org/10.1175/1520-0434(1998)013<0377:TWRA>2.0.CO;2

Futyan, J., & Del Genio, A. (2007). Deep convective system evolution over Africa and the tropical Atlantic. *Journal of Climate*, *20*(20), 5041–5060. https://doi.org/10.1175/JCLI4297.1

Giangrande, S. E., Collis, S., Theisen, A. K., & Tokay, A. (2014). Precipitation estimation from the ARM distributed radar network during the MC3E campaign. *Journal of Applied Meteorology and Climatology*, *53*(9), 2130–2147. https://doi.org/10.1175/JAMC-D-13-0321.1

Gorgucci, G., Chandrasekar, V., Bringi, V. N., & Scarchilli, G. (2002). Estimation of raindrop size distribution parameters from polarimetric radar measurements. *Journal of the Atmospheric Sciences*, *59*(15), 2373–2384. https://doi.org/10.1175/1520-0469(2002)059<2373:EORSDP>2.0.CO;2

Gunn, R., & Kinzer, G. D. (1949). The terminal velocity of fall for water droplets in stagnant air. *Journal of the Atmospheric Sciences*, *6*(4), 243–248. https://doi.org/10.1175/1520-0469(1949)006<0243:TTVOFF>2.0.CO;2

Haberlandt, U. (2007). Geostatistical interpolation of hourly precipitation from rain gauges and radar for a large-scale extreme rainfall event. *Journal of Hydrology*, *332*(14), 4–157.

Hossain, F., Anagnostou, E. N., Dinku, T., & Borga, M. (2004). Hydrological model sensitivity to parameter and radar rainfall estimation uncertainty. *Hydrological Processes*, *18*(17), 3277–3291. https://doi.org/10.1002/hyp.5659

Houze, R. A. Jr., Rasmussen, K. L., Zuluaga, M. D., & Brodzik, S. R. (2015). The variable nature of convection in the tropics and subtropics: A legacy of 16 years of the Tropical Rainfall Measuring Mission satellite. *Reviews of Geophysics*, *53*, 994–1021. https://doi.org/10.1002/2015RG000488

Illingworth, A. J., & Blackman, T. M. (2002). The need to represent raindrop size spectra as normalized gamma distributions for the interpretation of polarization radar observations. *Journal of Applied Meteorology*, *41*(3), 286–297. https://doi.org/10.1175/1520-0450(2002)041<0286:TNTRRS>2.0.CO;2

Jaffrain, J., & Berne, A. (2011). Experimental quantification of the sampling uncertainty associated with measurements from PARSIVEL disdrometers. *Journal of Hydrometeorology*, *12*(3), 352–370. https://doi.org/10.1175/2010JHM1244.1

Jaffrain, J., & Berne, A. (2012). Influence of the subgrid variability of the raindrop size distribution on radar rainfall estimators. *Journal of Applied Meteorology and Climatology*, *51*(4), 780–785. https://doi.org/10.1175/JAMC-D-11-0185.1

Jensen, M. P., Petersen, W. A., Bansemer, A., Bharadwaj, N., Carey, L. D., Cecil, D. J., et al. (2015). The midlatitude continental convective clouds experiment (MC3E). *Bulletin of the American Meteorological Society*, *97*(9), 1667–1686. https://doi.org/10.1175/BAMS-D-14-00228.1

Joss, J., & Waldvogel, A. (1967). Ein Spektrograph für Niederschlag strophen mit automatisher auswertung (A spectrograph for automatic measurement of rainfall). *Geofisica Pura e Applicata*, *68*(1), 240–246. https://doi.org/10.1007/BF00874898

Joss, J., & Waldvogel, A. (1969). Raindrop size distribution and sampling size errors. *Journal of the Atmospheric Sciences*, *26*(3), 566–569. https://doi.org/10.1175/1520-0469(1969)026<0566:RSDASS>2.0.CO;2

Joss, J., & Waldvogel, A. (1990). Precipitation measurement and hydrology. In D. Atlas (Ed.), *Radar in meteorology* (pp. 577–606). Boston: American Meteor Society. https://doi.org/10.1007/978-1-935704-15-7_39

Kalinga, O. A., & Gan, T. Y. (2006). Semi-distributed modelling of basin hydrology with radar and gauged precipitation. *Hydrological Processes*, *20*(17), 3725–3746. https://doi.org/10.1002/hyp.6385

Kathiravelu, G., Lucke, T., & Nichols, P. (2016). Rain drop measurement techniques: A review. *Water*, *8*(1), 29. https://doi.org/10.3390/w8010029

Kinnel, P. I. A. (1976). Some observations of the Joss-Waldvogel rainfall disdrometer. *Journal of Applied Meteorology*, *15*(5), 499–502. https://doi.org/10.1175/1520-0450(1976)015<0499:SOOTJW>2.0.CO;2

Klazura, G. E., Thomale, J. M., Kelly, D. S., & Jendrowski, P. (1999). A comparison of NEXRAD WSR-88D radar estimates of rain accumulation with gauge measurements for high- and low-reflectivity horizontal gradient precipitation events. *Journal of Atmospheric and Oceanic Technology*, *16*(11), 1842–1850. https://doi.org/10.1175/1520-0426(1999)016<1842:ACONWR>2.0.CO;2

Kozu, T., Iguchi, T., Shimomai, T., & Kashiwagi, N. (2009). Raindrop size distribution modeling from a statistical rain parameter relation and its application to the TRMM precipitation radar rain retrieval algorithm. *Journal of Applied Meteorology and Climatology*, *48*(4), 716–724. https://doi.org/10.1175/2008JAMC1998.1

Kozu, T., & Nakamura, K. (1991). Rain parameter estimation from dual-radar measurements combining reflectivity profile and path-integrated attenuation. *Journal of Atmospheric and Oceanic Technology*, *8*(2), 259–270. https://doi.org/10.1175/1520-0426(1991)008<0259:RPEFDR>2.0.CO;2

Kuligowski, R. J. (2010), GOES-R advanced baseline imager (ABI) algorithm theoretical basis document for rainfall rate (QPE). NOAA/NESDIS/STAR Rep., 44 pp. (https://www.goes-r.gov/products/ATBDs/baseline/Hydro_RRQPE_v2.0_no_color.pdf).

Kumjian, M. R., & Prat, O. P. (2014). The impact of raindrop collisional processes on the polarimetric radar variables. *Journal of the Atmospheric Sciences*, *71*(8), 3052–3067. https://doi.org/10.1175/JAS-D-13-0357.1

Maki, M., Keenan, T. D., Sasaki, Y., & Nakamura, K. (2001). Characteristics of the raindrop size distribution in tropical continental squall lines observed in Darwin, Australia. *Journal of Applied Meteorology*, *40*(8), 1393–1412. https://doi.org/10.1175/1520-0450(2001)040<1393:COTRSD>2.0.CO;2

Marshall, J. S., & Palmer, W. M. (1948). The distribution of raindrops with size. *Journal of Meteorology*, *5*(4), 165–166. https://doi.org/10.1175/1520-0469(1948)005<0165:TDORWS>2.0.CO;2

McFarquhar, G. M. (2004a). A new representation of collision-induced breakup of raindrops and its implications for the shapes of raindrop size distributions. *Journal of the Atmospheric Sciences*, *61*(7), 777–794. https://doi.org/10.1175/1520-0469(2004)061<0777:ANROCB>2.0.CO;2

McFarquhar, G. M. (2004b). The effect of raindrop clustering on collision-induced break-up of raindrops. *Quarterly Journal of the Royal Meteorological Society*, *130*(601), 2169–2190. https://doi.org/10.1256/qj.03.98

McFarquhar, G. M., & Heymsfield, A. J. (1996). Microphysical characteristics of three anvils sampled during the central equatorial Pacific experiment. *Journal of the Atmospheric Sciences*, *53*(17), 2401–2423. https://doi.org/10.1175/1520-0469(1996)053<2401:MCOTAS>2.0.CO;2

McFarquhar, G. M., & List, R. (1993). The effect of curve fits for the disdrometer calibration on rain drop spectra, rainfall rate and radar reflectivity. *Journal of Applied Meteorology*, *32*(4), 774–782. https://doi.org/10.1175/1520-0450(1993)032<0774:TEOCFF>2.0.CO;2

McFarquhar, G. M., Zhang, G., Poellot, M. R., Kok, G. L., McCoy, R., Tooman, T., et al. (2007). Ice properties of single-layer stratocumulus during the mixed-phase Arctic cloud experiment: 1. Observations. *Journal of Geophysical Research*, *112*, D24201. https://doi.org/10.1029/2007JD008633

Molini, A., Lanza, L. G., & La Barbera, P. (2005). The impact of tipping-bucket raingauge measurement errors on design rainfall for urban-scale applications. *Hydrological Processes*, *19*(5), 1073–1088. https://doi.org/10.1002/hyp.5646

North, K. W., Oue, M., Kollias, P., Giangrande, S. E., Collis, S., & Potvin, C. K. (2017). Vertical air motion retrievals in deep convective clouds using the ARM scanning radar network in Oklahoma during MC3E. *Atmospheric Measurement Techniques*, *10*, 1–33. https://doi.org/10.5194/amt-2016-269

Nzeukou, A., Sauvageot, H., Ochou, A. D., & Kebe, C. M. (2004). Raindrop size distribution and radar parameters at Cape Verde. *Journal of Applied Meteorology*, *43*(1), 90–105. https://doi.org/10.1175/1520-0450(2004)043<0090:RSDARP>2.0.CO;2

Parsons, D. A. (1941). Calibration of a weather bureau tipping-bucket Raingage. *Monthly Weather Review*, *69*(7), 205–205. https://doi.org/10.1175/1520-0493(1941)069<0205:COAWBT>2.0.CO;2

Pei, B., Testik, F. Y., & Gebremichael, M. (2014). Impacts of raindrop fall velocity and Axis ratio errors on dual-polarization radar rainfall estimation. *Journal of Hydrometeorology*, *15*(5), 1849–1861. https://doi.org/10.1175/JHM-D-13-0201.1

Press, W. H., Teukolsky, S. A., Vetterling, W. T., & Flannery, B. P. (1992). Numerical recipes in FORTRAN. In *The Art of Scientific Computing*, (2nd ed.pp. 678–683). New York: Cambridge Univ. Press.

Pruppacher, H. R., & Klett, J. D. (1996). *Microphysics of clouds and precipitation*, (2nd ed.p. 798). Dordrecht, Netherlands: Kluwer Acad.

Rosenfeld, D., Wolff, D. B., & Atlas, D. (1993). General probability-matched relations between radar reflectivity and rain rate. *Journal of Applied Meteorology*, *32*(1), 50–72. https://doi.org/10.1175/1520-0450(1993)032<0050:GPMRBR>2.0.CO;2

Ryzhkov, A., Diederich, M., Zhang, P., & Simmer, C. (2014). Potential utilization of specific attenuation for rainfall estimation, mitigation of partial beam blockage, and radar networking. *Journal of Atmospheric and Oceanic Technology*, *31*(3), 599–619. https://doi.org/10.1175/JTECH-D-13-00038.1

Sauvageot, H. (1994). Rainfall measurement by radar: A review. *Atmospheric Research*, *35*(1), 27–54. https://doi.org/10.1016/0169-8095(94)90071-X

Schumacher, C., & Houze, R. A. (2003). Stratiform rain in the tropics as seen by the TRMM precipitation radar. *Journal of Climate*, *16*(11), 1739–1756. https://doi.org/10.1175/1520-0442(2003)016<1739:SRITTA>2.0.CO;2

Seto, S., & Iguchi, T. (2015). Intercomparison of attenuation correction methods for the GPM dual-frequency precipitation radar. *Journal of Atmospheric and Oceanic Technology*, *32*(5), 915–926. https://doi.org/10.1175/JTECH-D-14-00065.1

Stenz, R., Dong, X., Xi, B., Feng, Z., & Kuligowski, R. J. (2016). Improving satellite quantitative precipitation estimation using GOES-retrieved cloud optical depth. *Journal of Hydrometeorology*, *17*(2), 557–570. https://doi.org/10.1175/JHM-D-15-0057.1

Stenz, R., Dong, X., Xi, B., & Kuligowski, R. J. (2014). Assessment of SCaMPR and NEXRAD Q2 precipitation estimates using Oklahoma Mesonet observations. *Journal of Hydrometeorology*, *15*(6), 2484–2500. https://doi.org/10.1175/JHM-D-13-0199.1

Testud, J., Oury, S., Black, R. A., Amayenc, P., & Dou, X. (2001). The concept of "normalized" distribution to describe raindrop spectra: A tool for cloud physics and cloud remote sensing. *Journal of Applied Meteorology*, *40*(6), 1118–1140. https://doi.org/10.1175/1520-0450(2001)040<1118:TCONDT>2.0.CO;2

Thurai, M., Gatlin, P., & Bringi, V. (2016). Separating stratiform and convective rain types based on the drop size distribution characteristics using 2D video disdrometer data. *Atmospheric Research*, *169*, 416–423. https://doi.org/10.1016/j.atmosres.2015.04.011

Tian, J., Dong, X., Xi, B., Wang, J., Homeyer, C. R., McFarquhar, G. M., & Fan, J. (2016). Retrievals of ice cloud microphysical properties of deep convective systems using radar measurements. *Journal of Geophysical Research: Atmospheres*, *121*, 10,820–10,839. https://doi.org/10.1002/2015JD024686

Tokay, A., Kruger, A., & Krajewski, W. F. (2001). Comparison of drop size distribution measurements by impact and optical disdrometers. *Journal of Applied Meteorology*, *40*(11), 2083–2097. https://doi.org/10.1175/1520-0450(2001)040<2083:CODSDM>2.0.CO;2

Tokay, A., Petersen, W. A., Gatlin, P., & Wingo, M. (2013). Comparison of raindrop size distribution measurements by collocated disdrometers. *Journal of Atmospheric and Oceanic Technology*, *30*(8), 1672–1690. https://doi.org/10.1175/JTECH-D-12-00163.1

Tokay, A., & Short, D. A. (1996). Evidence from tropical raindrop spectra of the origin of rain from Stratiform versus convective clouds. *Journal of Applied Meteorology*, *35*(3), 355–371. https://doi.org/10.1175/1520-0450(1996)035<0355:EFTRSO>2.0.CO;2

Trafalis, T., White, A., Santosa, B., & Richman, M. (2002). Data mining techniques for improved WSR-88D rainfall estimation. *Computers and Industrial Engineering*, *43*(4), 775–786. https://doi.org/10.1016/S0360-8352(02)00139-0

Ulbrich, C. W. (1983). Natural variations in the analytical form of the raindrop size distribution. *Journal of Applied Meteorology*, *22*(10), 1764–1775. https://doi.org/10.1175/1520-0450(1983)022<1764:NVITAF>2.0.CO;2

Ulbrich, C. W., & Atlas, D. (1998). Rainfall microphysics and radar properties: Analysis methods for drop size spectra. *Journal of Applied Meteorology*, *37*(9), 912–923. https://doi.org/10.1175/1520-0450(1998)037<0912:RMARPA>2.0.CO;2

Vivekanandan, J., Zhang, G., & Brandes, E. (2004). Polarimetric radar estimators based on a constrained gamma drop size distribution model. *Journal of Applied Meteorology*, *43*(2), 217–230. https://doi.org/10.1175/1520-0450(2004)043<0217:PREBOA>2.0.CO;2

Waldvogel, A. (1974). The N0 jump of raindrop spectra. *Journal of the Atmospheric Sciences*, *31*(4), 1067–1078. https://doi.org/10.1175/1520-0469(1974)031<1067:TJORS>2.0.CO;2

Wang, J., Dong, X., & Xi, B. (2015). Investigation of ice cloud microphysical properties of DCSs using aircraft in situ measurements during MC3E over the ARM SGP site. *Journal of Geophysical Research: Atmospheres*, *120*, 3533–3552. https://doi.org/10.1002/2014JD022795

Wang, J., Dong, X., Xi, B., & Heymsfield, A. J. (2016). Investigation of liquid cloud microphysical properties of deep convective systems: 1. Parameterization of raindrop size distribution and its application for stratiform rain estimation. *Journal of Geophysical Research: Atmospheres*, *121*, 10,739–10,760. https://doi.org/10.1002/2016JD024941

Xiao, R., & Chandrasekar, V. (1997). Development of a neural network based algorithm for rainfall estimation from radar measurements. *IEEE Transactions on Geoscience and Remote Sensing*, *36*, 160–171.

Xin, L., Reuter, G., & Larochelle, B. (1997). Reflectivity-rain rate relationships for convective rainshowers in Edmonton: Research note. *Atmosphere-Ocean*, *35*(4), 513–521. https://doi.org/10.1080/07055900.1997.9649602

Zhang, G., Vivekanandan, J., & Brandes, E. (2001). A method for estimating rain rate and drop size distribution from polarimetric radar measurements. *IEEE Transactions on Geoscience and Remote Sensing*, *39*(4), 830–841. https://doi.org/10.1109/36.917906

Zhang, G., Vivekanandan, J., & Brandes, E. (2003). The shape–slope relation in gamma raindrop size distributions: Statistical error or useful information? *Journal of Atmospheric and Oceanic Technology*, *20*(8), 1106–1119. https://doi.org/10.1175/1520-0426(2003)020<1106:TSRIOG>2.0.CO;2

Zhang, H., Zhang, Y., He, H., Xie, Y., & Zeng, Q. (2017). Comparison of raindrop size distributions in a midlatitude continental squall line during different stages as measured by Parsivel over East China. *Journal of Applied Meteorology and Climatology*, *56*(7), 2097–2111. https://doi.org/10.1175/JAMC-D-16-0336.1

Zhang, J., Howard, K., Langston, C., Kaney, B., Qi, Y., Tang, L., et al. (2016). Multi-Radar Multi-Sensor (MRMS) quantitative precipitation estimation: Initial operating capabilities. *Bulletin of the American Meteorological Society*, *97*(4), 621–638. https://doi.org/10.1175/BAMS-D-14-00174.1

Zhang, J., Howard, K., Langston, C., Vasiloff, S., Kaney, B., Arthur, A., et al. (2011). National mosaic and multi-sensor QPE (NMQ) system: Description, results, and future plans. *Bulletin of the American Meteorological Society*, *92*(10), 1321–1338. https://doi.org/10.1175/2011BAMS-D-11-00047.1